Electronic Supplementary Material (ESI) for RSC Advances.

Supporting Information

Intrinsic and Extrinsic Proton Conductivity in Metal-Organic Frameworks

S. Tominaka,[a,b*] and A. K. Cheetham[a*]

[a] *Department of Materials Science and Metallurgy, University of Cambridge, Charles Babbage Road, Cambridge CB3 0FS, United Kingdom. Fax: +44 1223 334567; Tel: +44 (0)1223 767061; E-mail: akc30@cam.ac.uk.*

[b] *International Center for Materials Nanoarchitectonics (WPI-MANA), National Institute for Materials Science (NIMS), Ibaraki 305-0044, Japan. Tel: +81 (0)29 860 4594; E-mail: TOMINAKA.Satoshi@nims.go.jp*

Contents

S1. Experimental details

Structure determinations. The crystal structure was determined by single crystal diffractometry using an Oxford Diffraction Gemini A Ultra X-ray diffractometer with Mo Kα radiation (λ = 0.71073 Å) operated at 50 kV and 40 mA. Data were collected under ambient conditions. Data collection, unit cell determination and refinement, absorption correction and data reduction were performed using the CrysAlisPro software from Agilent Technologies. An analytical absorption correction was performed by applying a face-based absorption correction as well as a spherical absorption correction.

The unit cell of 1 was indexed using twin finding function of the CrysAlisPro software. Then, the best matched cell was used for structure solution. The unit cell of **2** was indexed according to the reported lattice values of $[Fe(ox)(H_2O)_2]$.[1] Then, the data was reduced on the basis of the C2/c space group.

The Alert level A of the cif file of **2** is due to the presence of stacking faults (low quality data). The Alert level B of **1**, the big uncertainty in beta angle, is due to the presence of overlap peaks between twins.

Conductivity measurements. Conductivities were measured by the AC impedance method using an electrochemical instrument (Gamry Interface 1000) in the frequency range of 1 MHz to 0.01 Hz at an AC amplitude of 100 mV. For the single crystal measurements, the crystals were physically contacted with two Au microelectrodes (200 nm thick) having a 80 μm gap deposited on a SiO_2 chip as reported previously.[2] Using pressure sensitive silicone adhesive polyimide film (CMF-100-020W from MicroNova), crystals were gently picked up and mounted on the electrodes with their surface exposed to moisture. Humidity was controlled by mixing a water-saturated nitrogen gas and a dry nitrogen gas. The conductivity was measured along the long axis of crystals.

For the powder conductivity measurements, 100–130 mg of powder was gently ground using a pestle and mortar, and then was pressed into a pellet (1 cmϕ, 0.6–0.7 mm thick) at 0.5 GPa with a few drops of water. After drying under ambient conditions, the pellet was mounted in a closed powder conductivity measurement cell with stainless steel electrodes (EQ-STC 10 mm, MTI Corporation, USA) under saturated water vapour. Considering the pH value of the $[Fe(ox)(H_2O)_2]$-saturated solution (pH = 6.5–6.8 at 22°C), these electrodes are considered to work as blocking electrodes. The temperature was controlled by keeping the cell in an oven. AC impedance spectra were collected after equilibration time of >8 h with monitoring impedance spectra. At the first point, 90°C, resistance decreased for more than 2 days and the impedance spectra became stable.

AC impedance analyses. Impedance spectra were analyzed by curve fitting with equivalent circuits using the EchemAnalyst software from Gamry using equivalent circuits. The capacitance is calculated from constant phase element ($Z = Y^{-1}(j\omega)^{-\alpha}$), which is in general used for representing inhomogeneous response to the external electrical field. In order to obtain accurate conductivity values, impedance spectrum of the blank cell was measured (a resistance of 1.8 Ω with a series inductance of 1.7 μH).

In the powder impedance data, the complicated features found in the range of 10^{-2}–10^{4} Hz have a big capacitance of $>10^{-5}$ F (cf. the dry state has 1.6×10^{-10} F), these low frequency phenomena are attributable to electrode reactions, probably pseudo-capacitance of stainless steel electrodes. Thus, the impedance in the range of 10^{4}–10^{6} Hz is attributable to the bulk ion conduction. Since inductance originating from wires etc. has influence on this frequency range, in order to measure the resistance accurately, the spectra were analyzed by curve fitting using an equivalent circuit having a series inductance (Fig. S7).

Though the pressure does not affect, after the measurements, PXRD measurement indicates that **2** partially converted into **1**, as expected from the synthetic procedure (data not shown).

Powder diffraction. The PXRD samples were prepared by grinding the crystals gently using mortar and pestle for 1 min. The data was collected using a Bruker-AXS D8 diffractometer with Cu Kα radiation (λ = 1.5418 Å) in the Bragg–Brentano geometry. The patterns were analyzed by the Pawley fitting using the GSAS-II software,[3] and plotted with zero-shift correction and background subtraction.

Thermal analyses. Thermogravimetric analysis and differential scanning calorimetry were performed simultaneously using a TA Instruments Q600 SDT instrument with a nitrogen flow of 100 mL min^{-1} at a heating rate of 5 °C min^{-1}, from room temperature to 600°C.

Solubility test. 10 mg of **1** was soaked in 45 mL H_2O at RT or 90°C for 20 hours, then 40 mL of supernatant was dried at 90°C in air. 2 mg of black precipitate was recovered from the 90°C-treated one, while negligible yellow precipitate could be recovered from RT-treated one (the supernatant pH = 6.5–6.8 at 22°C, probably dominated by carbonate in air).

Synthesis of TTF nitrate. The tetrathiafulvalene (TTF) nitrate crystals were prepared by the oxidation reaction of TTF (97%, Sigma-Aldrich) by nitric acid (50 μL, 70%, Fisher) in N,N-dimethylformamide (DMF) (Fisher). In detail, TTF (20.5 mg) was dissolved in N,N-dimethylformamide (5 mL), and then was cooled down in a fridge (~6°C). Cooled nitric acid (~6°C) was gradually added to the solution, and then the solution was kept in the fridge for several days. Deep red needles, prisms and hexagonal plates were recovered by vacuum filtration, and rinsed with ethanol and chloroform. Though the morphologies are different, they have the same crystal structure, which was confirmed by single crystal X-ray diffraction and powder X-ray diffraction. The chemical composition was determined by elemental analysis at the Department of Chemistry, University of Cambridge (found, calcd., for $C_{12}H_8N_2O_6S_8$): C (27.15, 27.06), H(1.59, 1.51) and N (4.98, 5.26). CIF files are available (CCDC 1020095 and 1020096).

S2. Single crystal diffraction data

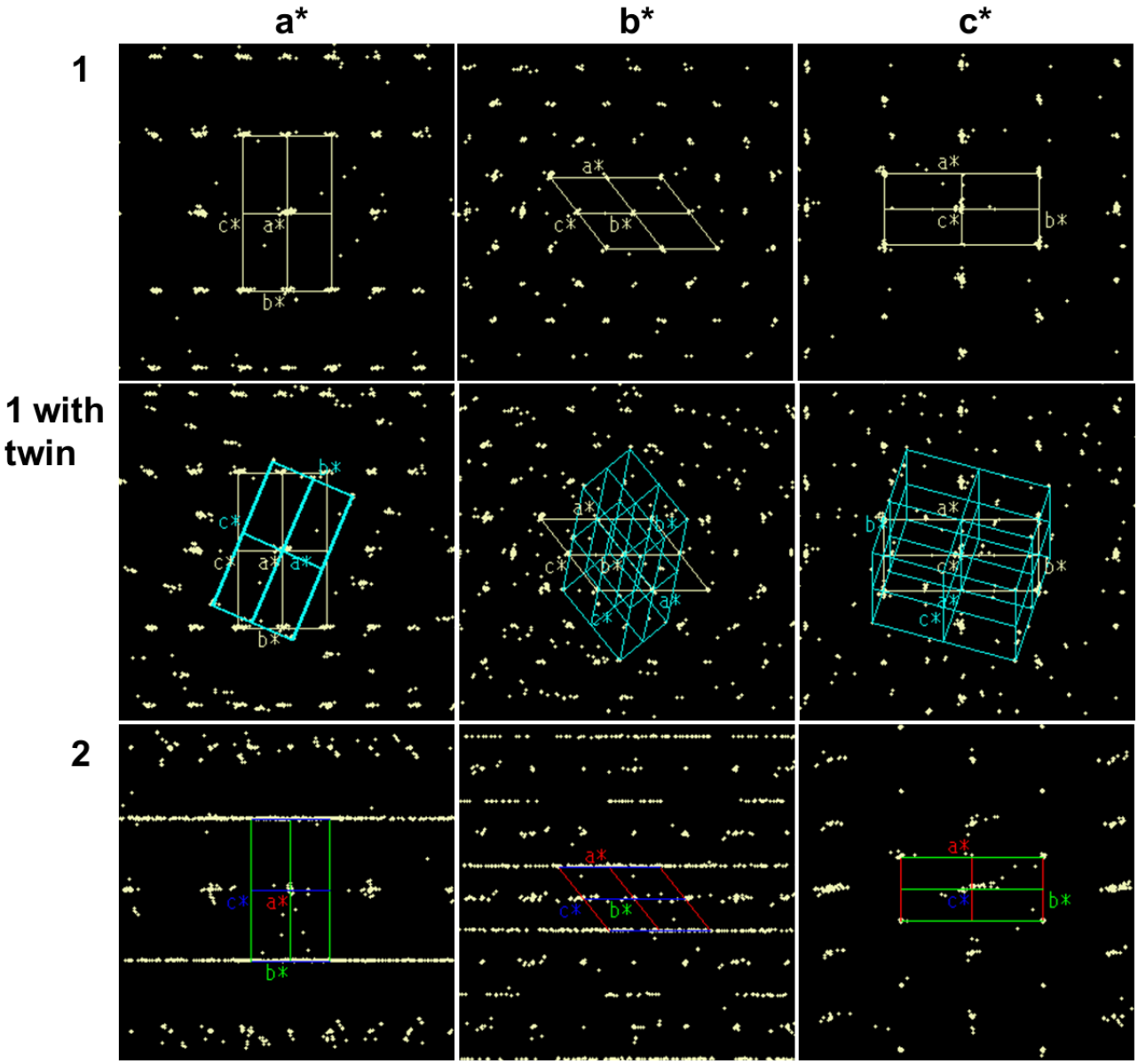

Figure S1 | Ewald sphere images obtained by single crystal diffraction. Top, sample 1. Middle, sample 2 with twin removal. Bottom, sample 2 (raw).

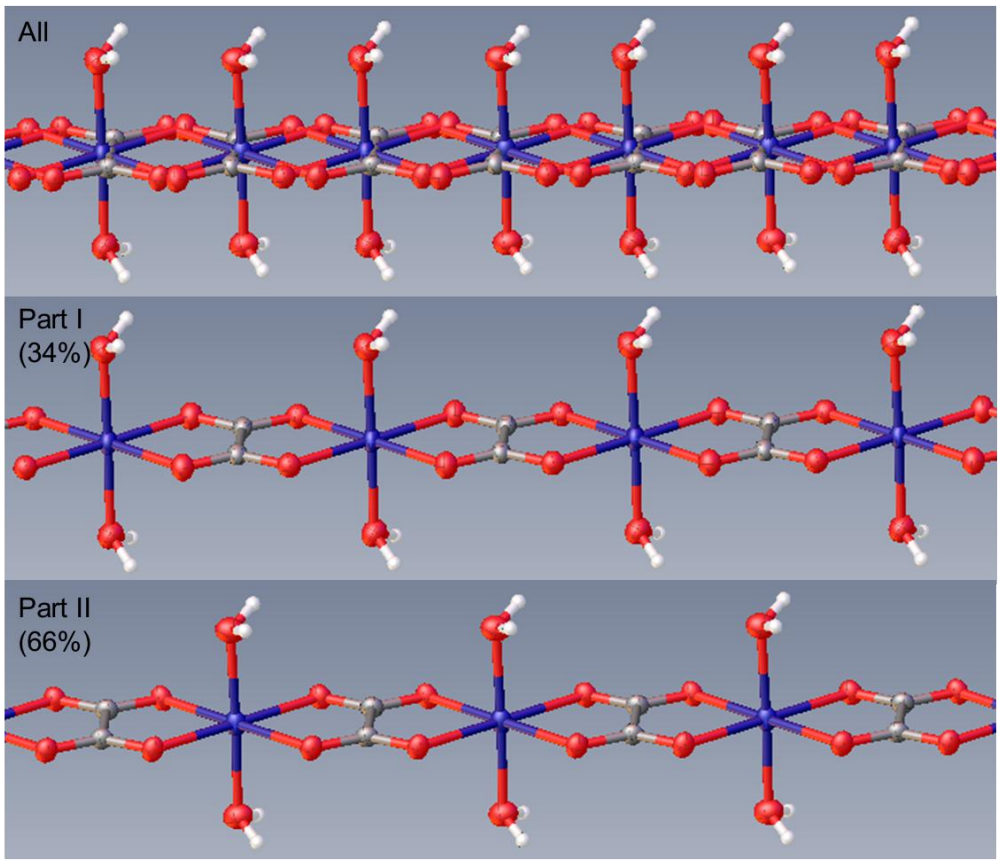

Figure S2 | Atom connectivity of **2** determined by the single crystal diffraction.

S3. Pawley fitting of PXRD patterns

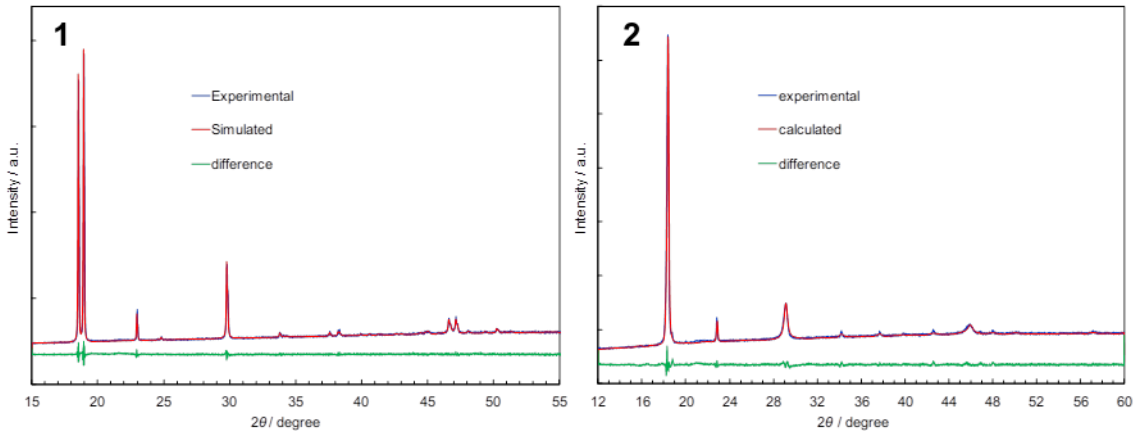

Figure S3 | Pawley fitting of PXRD patterns of [Fe(ox)$(H_2O)_2$] **1** and **2**.

Table S1 | Unit cells of [Fe(ox)$(H_2O)_2$] determined by X-ray diffraction

Sample	**1**	**1**	**2**	**2**	Literature[1]
Measurements	SXRD (Mo Kα)	PXRD (Cu Kα)	SXRD (Mo Kα)	PXRD (Cu Kα)	SXRD (Mo Kα)
Crystal system	Monoclinic	Monoclinic	Monoclinic	Monoclinic	Monoclinic
Space group	*C*2/*c*	–	*C*2/*c*	–	*C*2/*c*
a / Å	12.065(12)	12.0391(1)	12.209(4)	12.2113(4)	12.011(11)
b / Å	5.559(2)	5.5692(4)	5.5526(7)	5.5527(1)	5.557(5)
c / Å	9.817(9)	9.9393(1)	9.865(3)	9.8658(2)	9.920(9)
β (°)	128.03(15)	128.5353(6)	128.20(6)	128.207(2)	128.53(3)
V / Å^3	518.6(13)	521.29(4)	525.6(5)	525.65(2)	518.0(8)
d / g cm^{-3}	2.304	2.292	2.274	2.273	2.307
Temperature	293	RT	297	RT	293
Goodness of fit	R_1 = 8.79%, wR_2 = 24.06%, GOF = 1.307	R_w = 4.27%, Pawley fitting	R_1 = 10.9%, wR_2 = 25.78%, GOF = 1.246	R_w = 3.23%, Pawley fitting	R_1 = 3.74%, wR_2 = 9.31%, GOF = 1.387

S4. Crystal structure of TTF nitrate

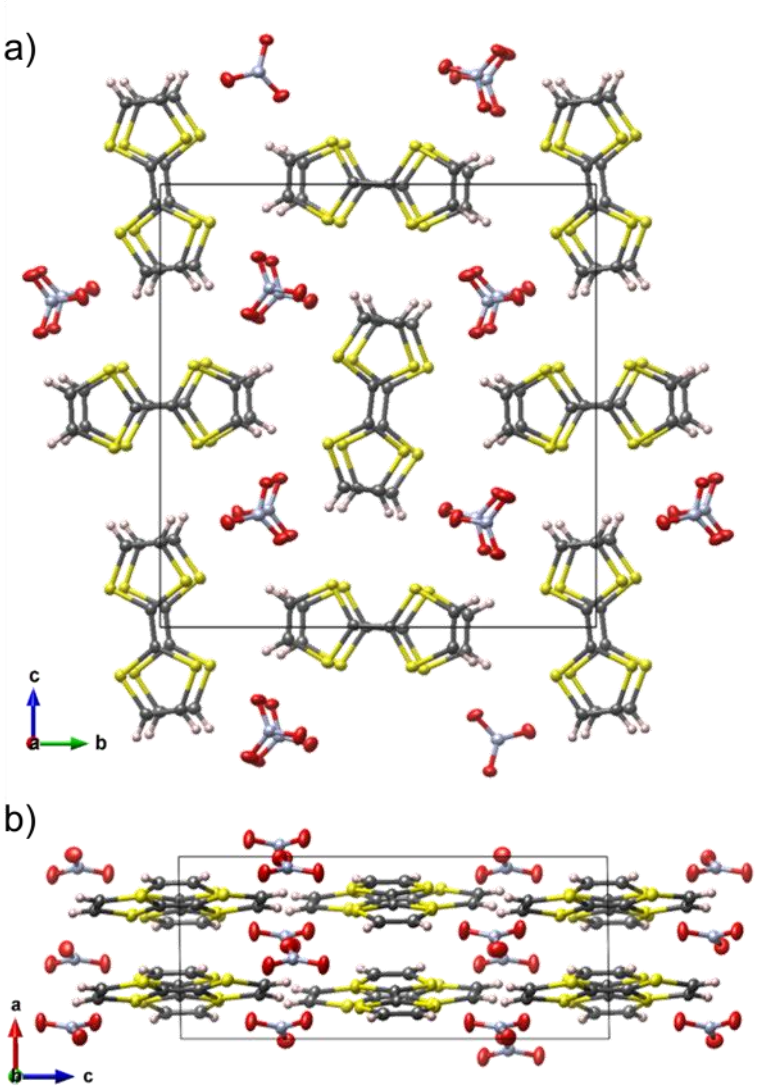

Figure S4 | Crystal structure of TTF nitrate at 120 K.

S5. Single-crystal AC impedance data

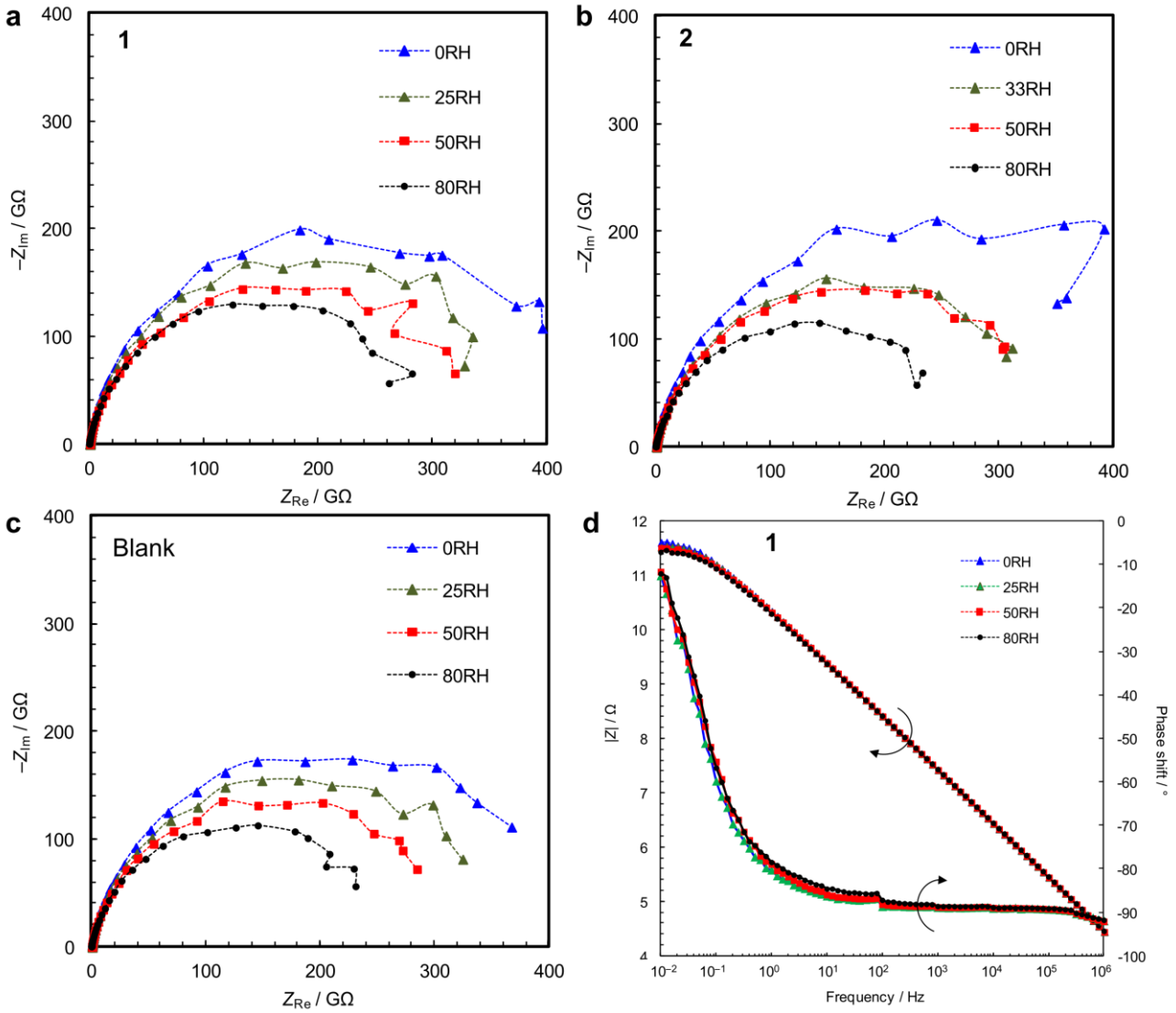

Figure S5 | Single-crystal impedance data. Complex-plane impedance diagrams of (**a**) [Fe(ox)(H_2O)$_2$] **1**, (**b**) [Fe(ox)(H_2O)$_2$] **2**, and (**c**) Blank cell. (**d**) Bode plot of **1**.

S6. Hydrogen bond networks in $[Fe(ox)(H_2O)_2]$

The negligible conductivity through the framework of **1** can be accounted for by considering hydrogen bond networks as follows. The frequencies of O–H stretching bands in infrared spectra are an indicator of the strength of hydrogen bonds and can be correlated to the O–O distances in the O–H···O hydrogen bonds.[4] In broad terms, O–O distances in the range 2.7–2.95 Å are preferred for proton conduction,[5] and these show O–H stretching bands around 3200–3500 cm^{-1}.[4] **1** contains such preferred hydrogen bonds having an O–O distance of 2.74 Å (Fig. S10a), to which the main sharp peak of O–H stretching at 3320 cm^{-1} (Fig. S10b) can be assigned. However, they are localized between water molecules and oxalate molecules in different $[Fe(ox)(H_2O)_2]$ chains as ox–H_2O–ox units. For long-range conduction, proton transport through ox–H_2O–ox units in the same chain is required. The O–O distance between water molecules and oxalate molecules in the same chains is 2.97–3.03 Å, to which the 3500 cm^{-1} shoulder can be assignable. This distance is far longer than the requirements for good proton mobility, thus the protons are localized in the interchain hydrogen bonds, as indicated by the IR intensity.

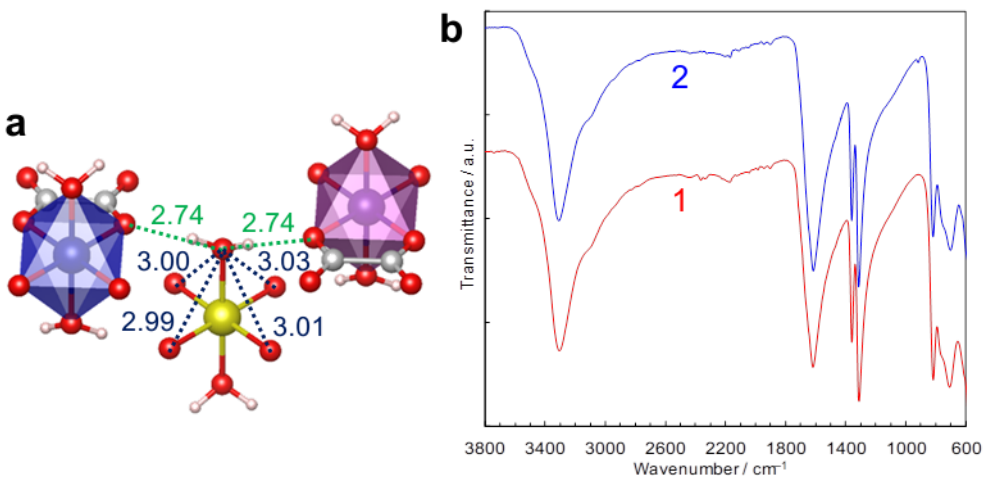

Figure S6 | Potential proton conduction paths in the $[Fe(ox)(H_2O)_2]$ framework. (**a**) The O–O distances in **1** determined by single crystal diffraction (in Å). (**b**) FT-IR spectrum of **1** and **2**.

S7. Powder AC impedance data and analyses

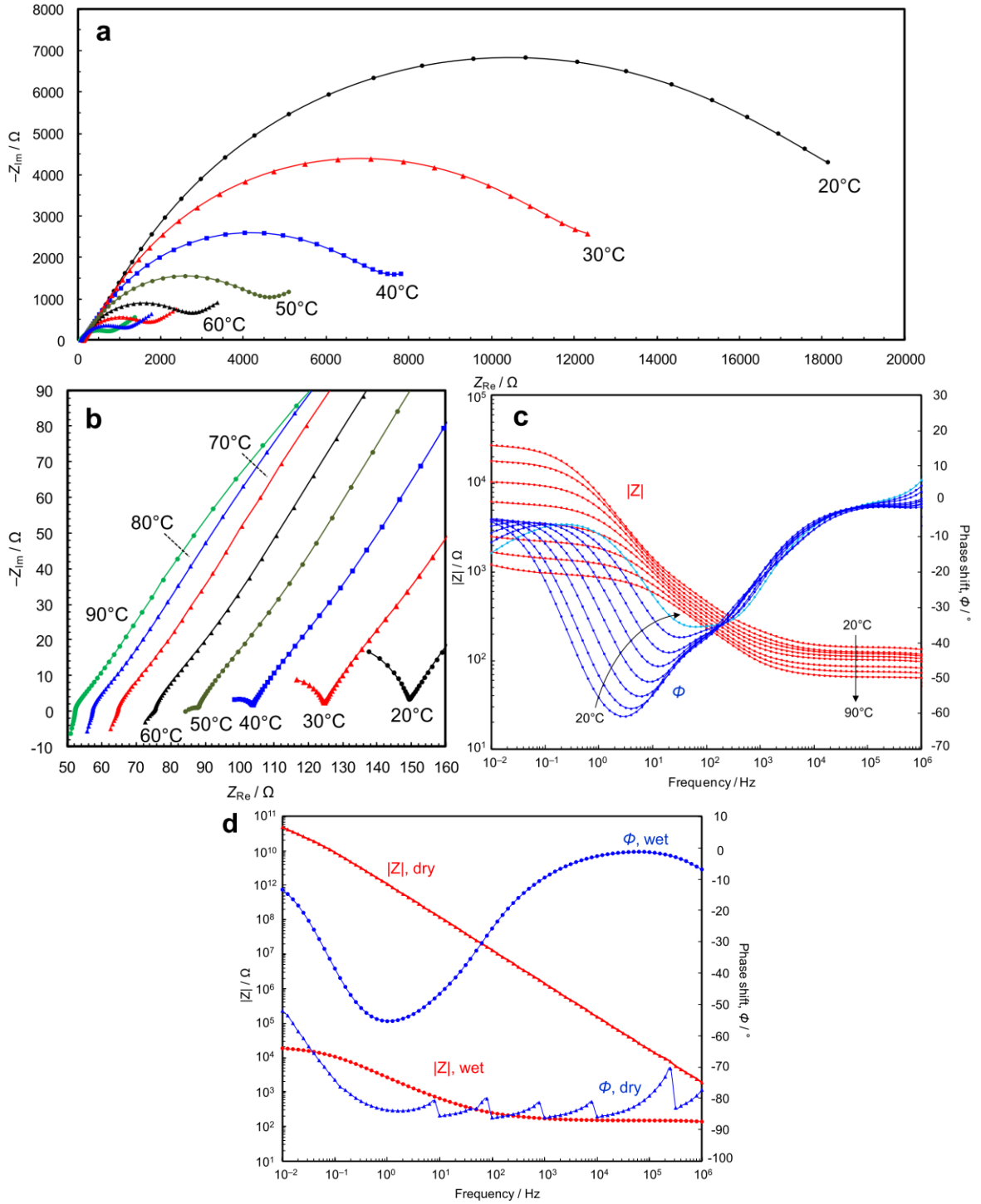

Figure S7 | Powder impedance data of $[Fe(ox)(H_2O)_2]$ **1**. **a,b** Complex-plane impedance diagrams. **c**, Bode plot, temperature dependence at 100%RH. **d**, Bode plot (20°C, 0%RH and 100%RH).

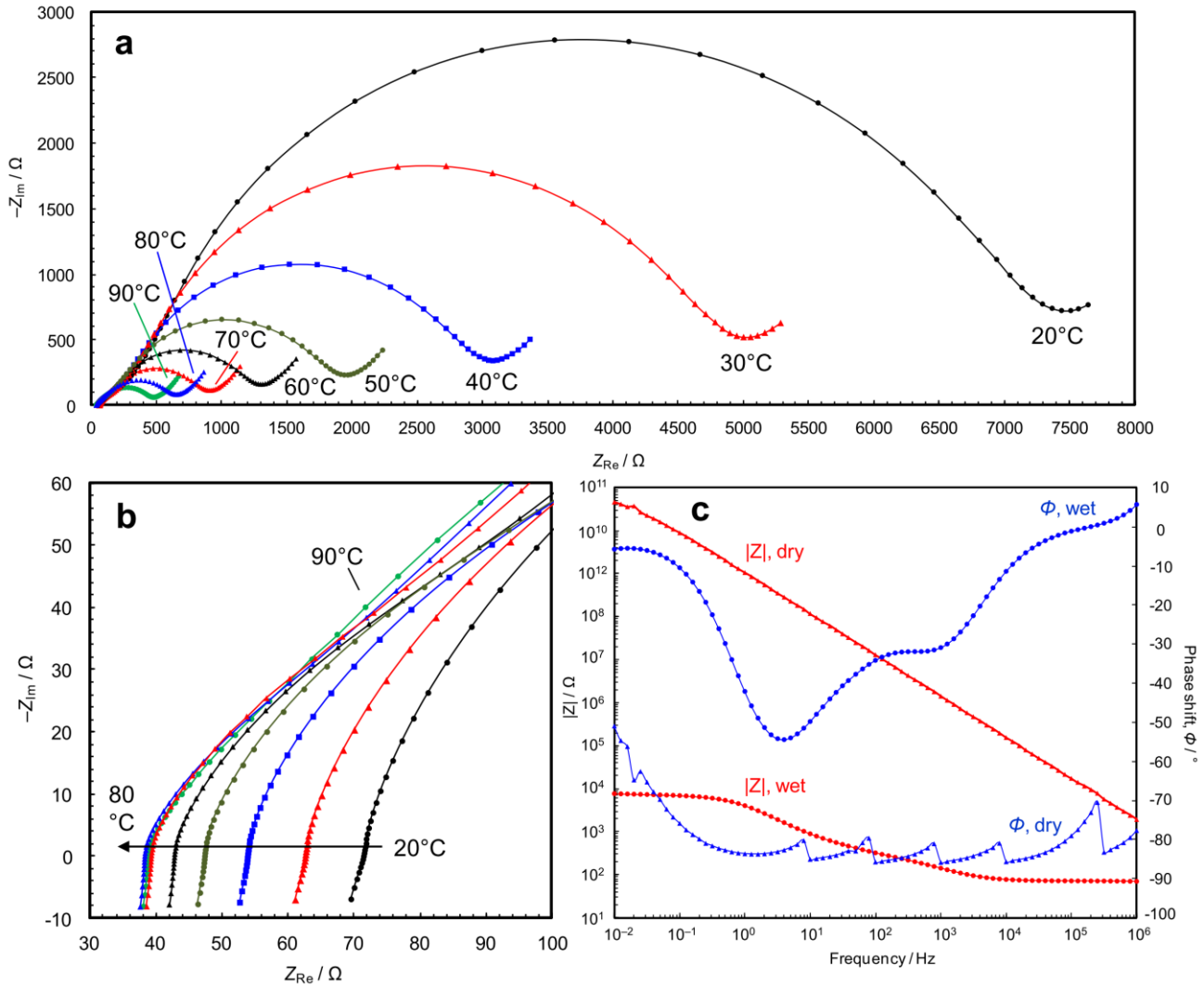

Figure S8 | Powder impedance data of [Fe(ox)(H_2O)$_2$] **2**. **a,b** Complex-plane impedance diagrams. **c**, Bode plot (20°C, 0%RH and 100%RH).

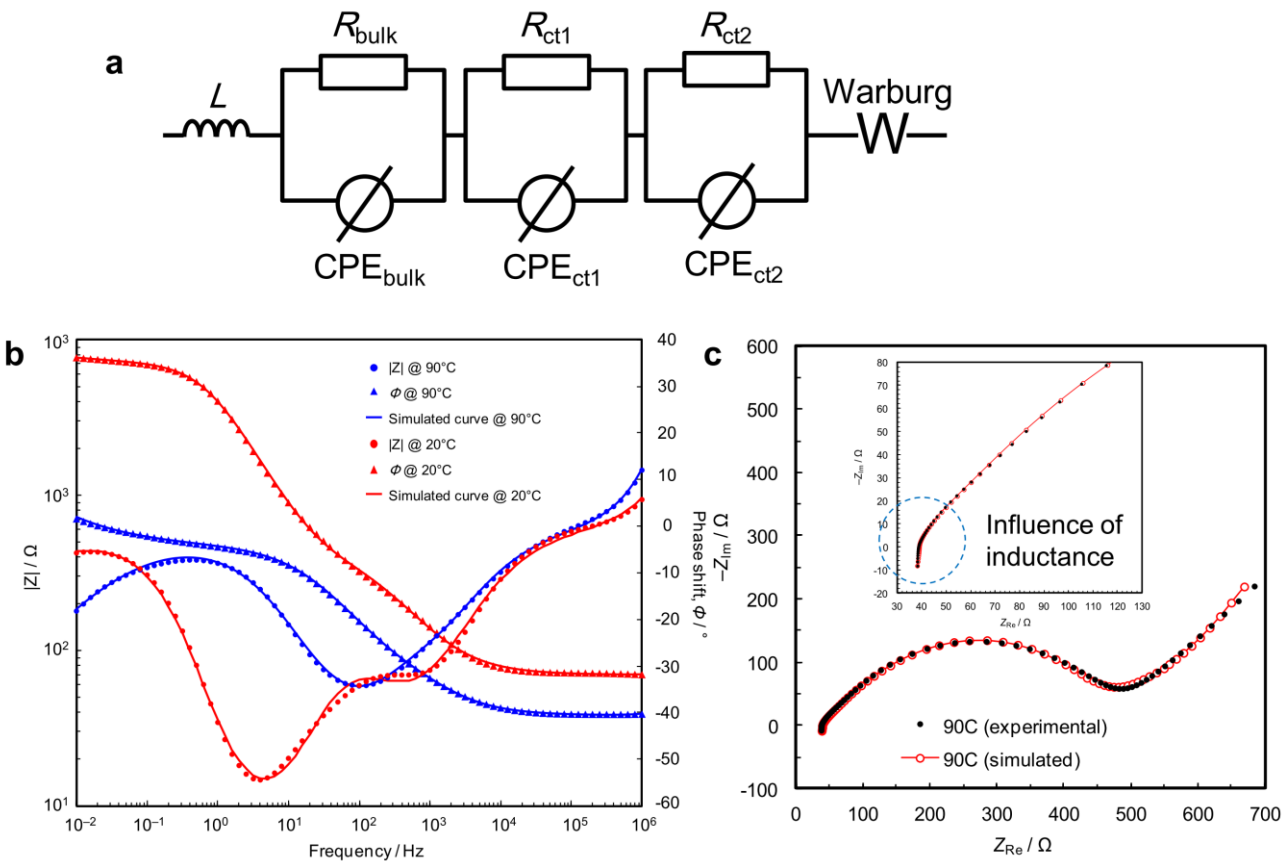

Figure S9 | Impedance data analysis of [Fe(ox)(H_2O)$_2$] **2** powder. (**a**) Equivalent circuit for representing bulk resistance R_{bulk} and capacitive behaviour CPE_{bulk} (CPE = constant phase element), two electrode reactions (R_{ct1}, CPE_{ct1}, R_{ct2} and CPE_{ct2}) probably attributable to pseudo-capacitive reactions on stainless steel surface, and a Warburg Impedance for the diffusion term associated with the electrode reactions. A inductance is used for representing parasitic inductance from cables and cells. Curve fitting in the Bode plots (**b**) and in the complex-plane impedance diagram (**c**). The high frequency region is often deformed due to the presence of the parasitic inductance, thus the use of inductance is important to obtain bulk resistance. The behaviour in this high frequency region, >10 kHz, depends on the capacitance or CPE_{bulk} and L, it is better to include L even when the behaviour looks a semicircle.

S8. Data for plotting Figure 5 and S8

There are two different Arrhenius equations,

$$\sigma T = \sigma_{01} \exp(-E_{a1}/RT) \quad \ldots(1)$$
$$\sigma = \sigma_{02} \exp(-E_{a2}/RT) \quad \ldots(2)$$

Where σ is conductivity, T is absolute temperature, E_a is activation energy, and R is the gas constant. The equation **1** is based on random theory, while equation **2** has not theoretical justification though it has been used widely.[6] Recently, equation **1** seems used more widely, especially in MOF community. In order to estimate σ_0 and E_a, the following Arrhenius plots are used.

$$\mathrm{Log}(\sigma T) = \mathrm{Log}(\sigma_{01}) - E_{a2}/(2.303RT) \quad \ldots(1')$$
$$\mathrm{Log}(\sigma) = \mathrm{Log}(\sigma_{02}) - E_{a2}/(2.303RT) \quad \ldots(2')$$

By linear approximation of these plots, values of σ_0 and E_a are obtained, but the values obtained using different plots are not exactly the same. The difference is the quasi-linear relation of Log(T) vs 1/T, which can be approximated as linear in narrow temperature range. Table S2 summarizes the difference of σ_0 and E_a in the different temperature range.

Using the values in Table S2, the σ_0 and E_a values obtained using equation **2'** were converted and summarized in Table S3 and S4.

Table S2 | Parameters for converting σ_0 and activation energy obtained by two different styles of Arrhenius plots

Temperature range (°C)	$\mathrm{Log}(\sigma_{01}) - \mathrm{Log}(\sigma_{02})$	$(E_{a1} - E_{a2})$ / meV	R^2
0–30	2.893	24.8	0.9998
0–60	2.917	26.2	0.9993
0–90	2.934	27.1	0.9986
0–100	2.940	27.5	0.9983
0–150	2.968	29.2	0.9967
0–200	2.994	30.9	0.9949
10–60	2.922	26.5	0.9995
10–90	2.941	27.6	0.9989
10–100	2.955	28.5	0.9987
10–150	2.983	30.3	0.9972
10–200	3.001	31.5	0.9955
20–60	2.929	26.9	0.9997
20–80	2.948	28.1	0.9994
20–90	2.948	28.1	0.9992
20–100	2.955	28.5	0.9990
20–150	2.893	30.3	0.9977
20–200	3.009	32.0	0.9961

Table S3 | σ_0 and E_a of MOF-based proton conductors.

Name	Type	Log(σ_0 / S cm^{-1}K^{-1})	E_a / eV	σ / S cm^{-1}	T / K	Reference (DOI)
[Fe(ox)(H_2O)$_2$](**1**)	Dense	2.31	0.17	5.7×10^{-4}	293	This work
[Fe(ox)(H_2O)$_2$](**2**)	Dense	2.05	0.14	1.5×10^{-3}	293	This work
[Fe(ox)(H_2O)$_2$]	Dense	5.84	0.37	1.3×10^{-3}	298	10.1021/ja808681m
[Mn(dhbq)(H_2O)$_2$]	Dense	2.45	0.26	4.0×10^{-5}	300	10.1246/cl.2009.654
(HOC_2H_4)$_2$-dtoa-Cu	Dense	0.01	0.19	2.2×10^{-6}	300	10.1246/bcsj.52.3296
(NH_4)$_2$(adp)[Zn_2(ox)$_3$]·3H_2O	Layered	11.03	0.63	8.0×10^{-3}	298	10.1021/ja9040016
PCMOF3	Layered	1.31	0.19	3.5×10^{-5}	298	10.1021/ja107035w
Ca-SBBA	Layered	1.30	0.23	8.6×10^{-6}	298	10.1039/c2cc31135f
Sr-SBBA	Layered	7.59	0.56	4.4×10^{-5}	298	10.1039/c2cc31135f
[Al(OH)(14bdc)]·H_2O, **MIL-53(Al)**	Porous	2.78	0.47	2.3×10^{-8}	298	10.1021/ja109810w
[Al(OH)(14bdc-NH_2)]·H_2O, **MIL-53(Al)-NH_2**	Porous	2.45	0.45	2.3×10^{-8}	298	10.1021/ja109810w
[Al(OH)(14bdc-OH)]·1.5H_2O, **MIL-53(Al)-OH**	Porous	0.66	0.27	4.2×10^{-7}	298	10.1021/ja109810w
[Fe(OH)(14bdc-(CO_2H)$_2$)]·H_2O, **MIL-53(Fe)-(CO_2H)$_2$**	Porous	0.33	0.21	2.0×10^{-6}	298	10.1021/ja109810w
[$Mo_5P_2O_{23}$][Cu(phen)(H_2O)]$_3$·5H_2O	Porous	1.67	0.23	2.2×10^{-5}	301	10.1039/c1cc15162b
[In(5TIA)$_2$]·($NH_2(CH_2)_2$)(H_2O)	Porous	0.50	0.137	5.35×10^{-5}	301	10.1039/c2cc31527k
[In(13bdc)$_2$]·$N(CH_3)_4$	Porous	6.69	0.47	2.2×10^{-4}	301	10.1039/c2cc31527k
[Cd(5TIA)$_2$]·2($NH_2(CH_2)_2$)(H_2O)	Porous	2.76	0.163	3.61×10^{-3}	301	10.1039/c2cc31527k
(NH_4)$_4$[$MnCr_2$(ox)$_6$]·4H_2O	Porous	3.40	0.23	1.1×10^{-3}	298	10.1021/ja206917z
PCMOF-5(98%RH)	Porous	2.75	0.19	2.5×10^{-3}	333	10.1021/ja310435e
PCMOF-5(90%RH)	Porous	3.75	0.35	2.0×10^{-5}	293	10.1021/ja310435e
Prussian blue	Porous	3.33	0.22	1.2×10^{-3}	293	10.1021/ja1003851
[Zn(l-L_{Cl})(Cl)]·2H_2O	Porous	3.77	0.34	4.45×10^{-5}	304	10.1021/ja2078637
[La($dtmpH_5$)]·7H_2O	Porous	4.98	0.275	8.0×10^{-3}	301	10.1039/c2dt11992g
[Ca(135btcH)(H_2O)]·H_2O **Ca-BTC-H_2O**	Porous	1.60	0.18	1.2×10^{-4}	298	10.1039/c2cc34006b
Ca-PiPh-tA-I	Porous	3.13	0.23	5.7×10^{-4}	297	10.1021/ja500356z
Ca-PiPh-tA-II	Porous	4.46	0.32	3.6×10^{-4}	297	10.1021/ja500356z
Im@[Al(OH)(14ndc)]	Anhydrous	5.63	0.6	2.2×10^{-5}	393	10.1038/nmat2526
Im@Al[OH)(14bdc)], **Im@MIL-53(Al)**	Anhydrous	7.13	0.9	1.0×10^{-7}	393	10.1038/nmat2526
His@Al[OH)(14ndc)]	Anhydrous	2.83	0.25	1.7×10^{-3}	423	10.1002/anie.201102997
Tz@βPCMOF2	Anhydrous	5.36	0.54	2.0×10^{-4}	423	10/1038/NCHEM.402
[Zn(H_2PO_4)$_2$(Tz)$_2$] (Tz = 1,2,4-Triazole)	Anhydrous	6.21	0.63	1.2×10^{-4}	423	10.1021/ja304693r

Table S4 | σ_0 and E_a of classical solid-state proton conductors[a]

Name	Type	Conduction path	Log(σ_0 / S cm^{-1}K^{-1})	E_a / eV	σ / S cm^{-1}	T / K	Reference (DOI)
H_2O (ice)	Dense	Defect	6.57	0.576	1.0×10^{-7}	260	10.1017/CBO9780511524806.004
KH_2PO_4	Dense	Defect	4.48	0.596	1.0×10^{-8}	300	10.1017/CBO9780511524806.004
KH_2AsO_4	Dense	Defect	5.99	0.686	1.0×10^{-8}	300	10.1017/CBO9780511524806.004
BYZ = $BaZr_{0.8}Y_{0.2}O_{3-\delta}$	Dense	Defect	6.47	0.696	1.1×10^{-1}	773	10.1038/NMAT2837
β-Alumina (NH_4^+)	Dense	Cation sites	5.48	0.526	1.5×10^{-6}	300	10.1017/CBO9780511524806.004
β-Alumina (H_3O^+), dried	Dense	Cation sites	6.34	0.826	1.0×10^{-10}	300	10.1017/CBO9780511524806.004
$H_3O{\cdot}[Zr_2(PO_4)_3]$, **NASICON**	Dense	Cation sites	6.31	0.586	1.0×10^{-6}	300	10.1017/CBO9780511524806.004
$(H_3O)_5[GdSi_4O_{12}]$	Dense	Cation sites	4.97	0.506	1.0×10^{-6}	300	10.1017/CBO9780511524806.004
$H_3O{\cdot}ClO_4$	Dense	Rotational disorder	4.31	0.316	3.4×10^{-4}	300	10.1017/CBO9780511524806.004
$CsHSO_4$ (420K)	Dense	Rotational disorder	4.89	0.356	1.0×10^{-2}	420	10.1017/CBO9780511524806.004
$[H_3PW_{12}O_{40}]{\cdot}21H_2O$, **Polyoxometalate**	Dense	H_2O network	7.40	0.426	6.0×10^{-3}	300	10.1017/CBO9780511524806.004
$[H_3SiW_{12}O_{40}]{\cdot}28H_2O$, **Polyoxometalate**	Dense	H_2O network	8.10	0.426	3.0×10^{-2}	300	10.1017/CBO9780511524806.004
$[H_3PMo_{12}O_{40}]{\cdot}29H_2O$, **Polyoxometalate**	Dense	H_2O network	4.66	0.176	1.7×10^{-1}	300	10.1017/CBO9780511524806.004
$H_3O{\cdot}[UO_2PO_3]{\cdot}3H_2O$	Layered	Interlayer, water-assisted	6.46	0.376	5.0×10^{-3}	301	10.1017/CBO9780511524806.004
α-$Zr(HPO_4)_2{\cdot}H_2O$	Layered	Interlayer, water-assisted	2.98	0.326	1.0×10^{-5}	298	10.1002/9781119962502.ch10
$Ce(HPO_4){\cdot}3.8H_2O$	Layered	Interparticle phase	2.08	0.196	2.0×10^{-4}	298	10.1017/CBO9780511524806.004
Zeolite A (NH^{4+}), 10.8 wt% H_2O	Porous	Micropores	8.08	0.63	1.1×10^{-5}	300	10.1016/0025-5408(82)90106-4
Nafion™	Polymer	Water channel	5.30	0.246	5.0×10^{-2}	300	10.1017/CBO9780511524806.004
BMITf@Nafion	Anhydrous polymer	Ionic liquid network	4.26	0.231	1.1×10^{-1}	453	10.1149/1.1393153
Imidazole@SPEK	Anhydrous polymer	Imidazole network	3.80	0.282	1.3×10^{-1}	473	10.1016/S0013-4686(97)10031-7
$SnO_2{\cdot}2H_2O$	Gel	Interparticle phase	2.87	0.226	4.0×10^{-4}	300	10.1017/CBO9780511524806.004
$Sb_2O_5{\cdot}5.4H_2O$	Gel	Interparticle phase	3.47	0.186	7.5×10^{-3}	300	10.1017/CBO9780511524806.004
$HClO_4{\cdot}5.5H_2O$ (liquid)	Liquid	H_2O network	3.72	0.046	3.0	300	10.1017/CBO9780511524806.004

BMITf = 1-butyl, 3methyl imidaxolium trifluoromethane sulfonate (ionic liquid). SPEK = sulfonated polyetherketone.

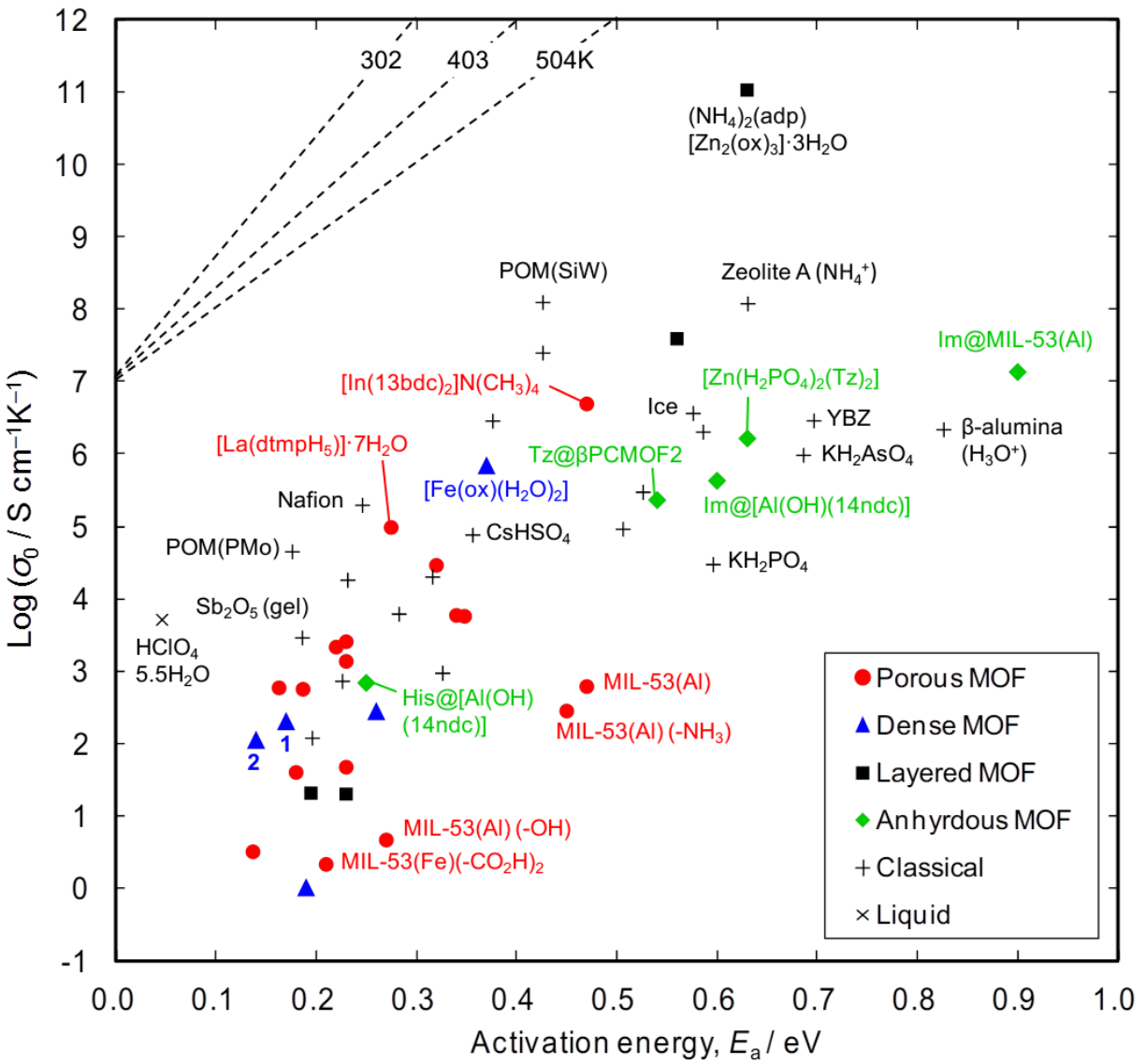

Figure S10 | Comparison of proton conductivity in metal-organic frameworks (MOFs) and classical solid-state materials. Relationship between the pre-exponential factor σ_0 of the Arrhenius Equation and the activation energy E_a are plotted. The top left dotted lines show the gradients where conductivity values of different materials are the same (302, 403 and 504 K). MIL-53(M) is [M(OH)(14bdc)], where bdc is benzenedicarboxylic acid. Im@, His@ and Tz@ mean incorporation of imidazole, histamine and 1,2,4-triazole molecules, respectively. $-NH_3$, -OH and $-CO_2H$ mean functional groups of modified bdc molecules. 14ndc = 1,4-naphthalenedicarboxylic acid. dtmp = hexamethylenediamine tetra(methylenephosphonic acid). adp = adipic acid. POM = polyoxometalate ($H_3PMo_{12}O_{40}$•$29H_2O$ or $H_3SiW_{12}O_{40}$•$28H_2O$). YBZ = yttrium-doped barium zirconate.

S9. Thermogravimetric analyses

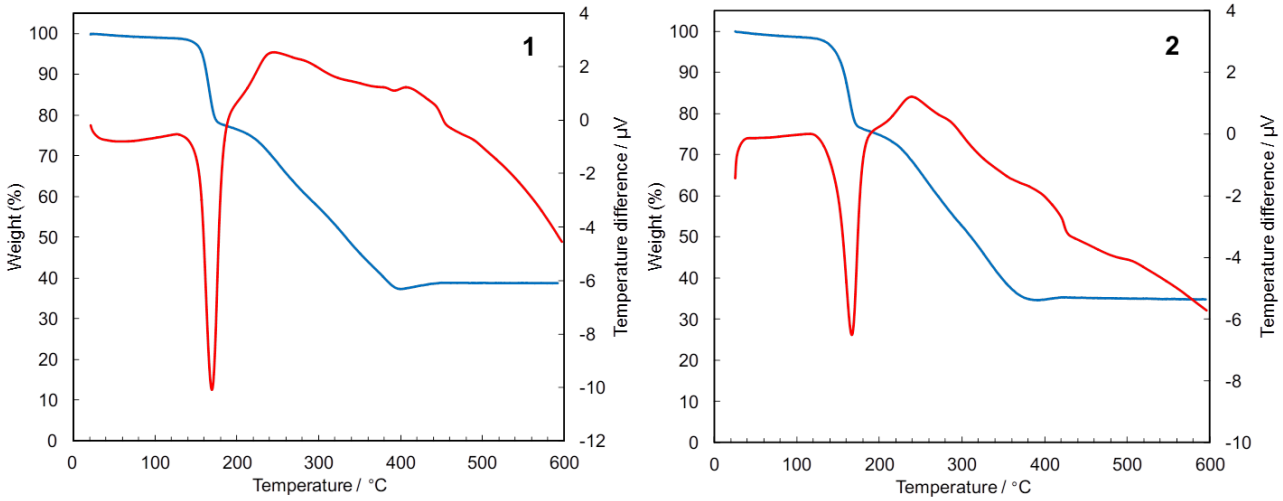

Figure S11 | Thermogravimetric analysis of $[Fe(ox)(H_2O)_2]$ 1 and 2. Simultaneous differential scanning calorimetry (DSC)-thermogravimetric analysis (TGA) recorded with N_2 flow of 100 mL min^{-1} at scan rate of 5 °C min^{-1}.

Refefences

1. Echigo T, Kimata M. Single-crystal X-ray diffraction and spectroscopic studies on humboldtine and lindbergite: weak Jahn-Teller effect of Fe2+ ion. *Physics and Chemistry of Minerals* 2008, **35**(8)**:** 467-475.

2. Tominaka S, Henke S, Cheetham AK. Coordination polymers of alkali metal trithiocyanurates: structure determinations and ionic conductivity measurements using single crystals. *CrystEngComm* 2013, **15**(45)**:** 9400-9407.

3. Toby BH, Von Dreele RB. GSAS-II: the genesis of a modern open-source all purpose crystallography software package. *J Appl Cryst* 2013, **46:** 544-549.

4. Novak A. Hydrogen bonding in solids correlation of spectroscopic and crystallographic data. *Large Molecules*, vol. 18. Springer, 1974, pp 177-216.

5. Potier A. The hydrogen bond and chemical parameters favouring proton mobility in solids. In: Colomban P (ed). *Proton conductors: Solids, membranes and gels (materials and devices)*. Cambridge University Press: Cambridge, 1992, pp 1-17.

6. Bruce PG (ed). *Solid State Electrochemistry*. Cambridge University Press: Cambridge, 1995.